Temporal and spectral manipulations of correlated photons using a time lens

Sunil Mittal,[1,2,*] Venkata Vikram Orre,[1,2] Alessandro Restelli,[1] Reza Salem,[3] Elizabeth A. Goldschmidt,[1,4] and Mohammad Hafezi[1,2]

[1]*Joint Quantum Institute, NIST/University of Maryland, College Park, Maryland 20742, USA*

[2]*Department of Electrical and Computer Engineering and IREAP, University of Maryland, College Park, Maryland 20742, USA*

[3]*PicoLuz, LLC, Jessup, Maryland 20794, USA*

[4]*U.S. Army Research Laboratory, Adelphi, Maryland 20783, USA*

(Received 13 April 2017; published 4 October 2017)

A common challenge in quantum information processing with photons is the limited ability to manipulate and measure correlated states. An example is the inability to measure picosecond-scale temporal correlations of a multiphoton state, given state-of-the-art detectors have a temporal resolution of about 100 ps. Here, we demonstrate temporal magnification of time-bin-entangled two-photon states using a time lens and measure their temporal correlation function, which is otherwise not accessible because of the limited temporal resolution of single-photon detectors. Furthermore, we show that the time lens maps temporal correlations of photons to frequency correlations and could be used to manipulate frequency-bin-entangled photons. This demonstration opens a new avenue to manipulate and analyze spectral and temporal wave functions of many-photon states.

DOI: 10.1103/PhysRevA.96.043807

I. INTRODUCTION

Photons entangled in spectral-temporal degrees of freedom are extremely advantageous for robust, long-distance entanglement distribution [1–4]. This characteristic feature has led to the development of a variety of techniques for spectral and temporal manipulations of single photons [5–12]. Recently, spectral compression of photons has gained widespread attention in order to efficiently interface wideband sources of correlated photons with narrowband nodes of a quantum network, for example, quantum dots and atomic systems [11,13–15]. At the same time, temporal magnification of photons facilitates high-fidelity photonic measurements in quantum simulations [16–19]. For example, on-chip temporal boson sampling and quantum walks [20–24] can have photonic wave packets with temporal features shorter than the resolution of existing single-photon detectors [25–27].

A versatile approach to spectrally compress and temporally magnify single photons is to use time-lens techniques [28]. While time lensing has been used widely in the past for temporal magnification of classical light pulses [29–31], its use for single photons is very recent. Specifically, time-lens-based techniques have demonstrated spectral manipulations of single photons [14,15,32] and also time-resolved detection of a single photon arriving in two time bins [33]. However, these demonstrations have manipulated only single photons. It is highly desirable to manipulate and also measure temporal and spectral correlations of multiphoton states.

In this work, we use an electro-optic phase modulator (EOM)-based time lens to magnify the two-photon temporal wave function associated with time-bin-entangled photons while simultaneously preserving their quantum correlations. Our time lens is designed to work in the telecom domain and achieves a temporal magnification of 9.6(2)×. First, we use this magnification to resolve two photons with a delay much less than the resolution of our superconducting nanowire single-photon detectors (SNSPDs). Then, we measure the joint-temporal intensity (JTI) of the magnified two-photon wave function, which is otherwise not measurable because of the limited detector resolution, and distinguish correlations between bunched and antibunched time-bin-entangled photon pairs. Finally, we show that the time lens maps temporal correlations of incoming photons to frequency correlations of outgoing photons and can be used to manipulate frequency-bin-entangled two-photon states [34].

II. TIME-LENS SETUP

Figure 1 illustrates a schematic of our time-lens setup. A dispersive element with a group delay dispersion (GDD) $\phi_i^{''} = \frac{d^2\phi_i(\omega)}{d\omega^2}$ is first used to spectrally chirp the input photon pulses. Here ω is the angular frequency, and $\phi_i(\omega)$ is the frequency-dependent phase shift accumulated during propagation. A time lens is then implemented using an EOM driven with a rf field of angular frequency ω_m and amplitude V_m. It imposes a time-varying phase shift $\phi_l(t) = -\frac{\pi V_m}{V_\pi}\cos(\omega_m t)$, where V_π is the π phase-shift voltage. When $\omega_m t \ll 1$ and the time of arrival of photons is locked to the phase of the rf drive, the phase shift can be approximated as $\phi_l(t) = \frac{\pi V_m}{2V_\pi}\omega_m^2 t^2$, with the corresponding GDD $\phi_l^{''} = \frac{V_\pi}{\pi V_m \omega_m^2}$. This quadratic time-varying phase introduced by the time lens is exactly analogous to the spatially varying phase imposed by a spatial lens [28]. Furthermore, similar to a spatial lens which introduces transverse momentum shift because of its curvature, the quadratic phase modulation and the associated GDD in a time lens result in a linear frequency shift between two photons incident on the time lens with a delay δt_{in}, given by

$$\delta\nu = \frac{V_m}{V_\pi}\frac{\omega_m^2}{2}\delta t_{\text{in}}. \tag{1}$$

Therefore, the time lens linearly maps the information contained in the temporal degree of freedom of photons to the frequency domain. This is again analogous to the action of a spatial lens which Fourier transforms spatial information about an object to the momentum domain. Finally, photons are subject to a large GDD at the output $\phi_o^{''}$, where the frequency

*mittals@umd.edu

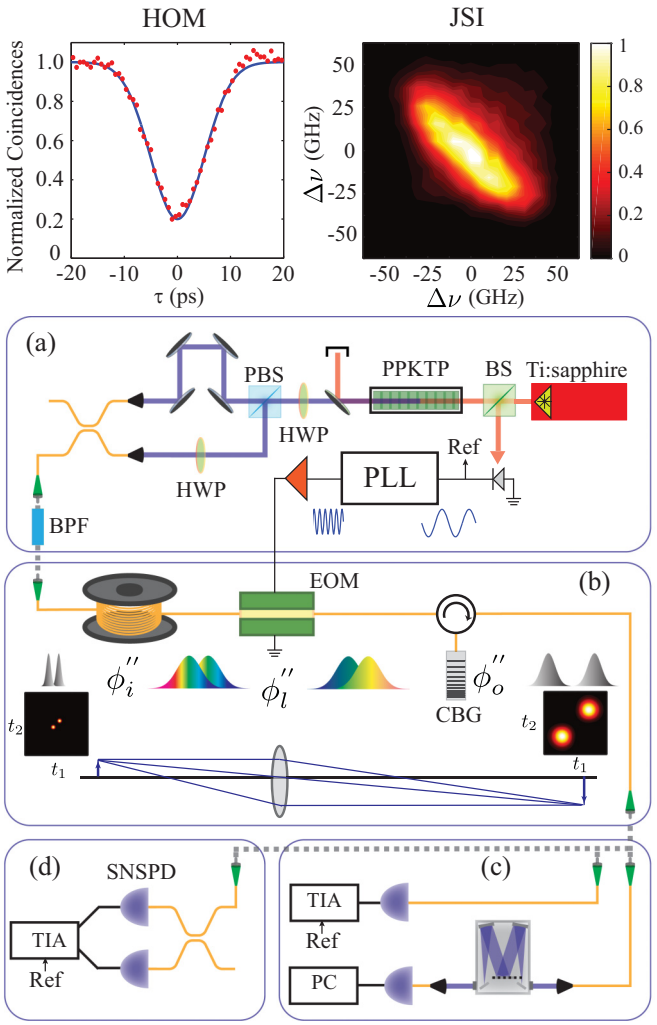

FIG. 1. (a) Time-bin-entangled photons are generated using type-II SPDC and a combination of a half-wave plate (HWP), a polarization beam splitter (PBS), and a delay line. Insets show the measured HOM interference with a visibility of ≈80% and nearly symmetric joint-spectral intensity (JSI), after the bandpass filter (BPF). The relative phase θ introduced by the delay line was stabilized using interference of another cw laser. (b) A converging time lens is implemented using 15 km of SMF-28 fiber, an electro-optic phase modulator (EOM), and a chirped Bragg grating (CBG) which emulates 150 km of SMF-28 fiber. (c) A SNSPD and a time-interval analyzer (TIA) are used for single-channel time-resolved detection of photons. A monochromator, along with a SNSPD and a photon counting circuit, is used for spectral measurements. (d) For JTI measurements, the output of the time lens is fed to a fused-fiber beam splitter connected to two SNSPDs and a time-tagged coincidence counting electronics.

shift $\delta\nu$ leads to a differential delay $2\pi\delta\nu\phi_o''$. The total delay between the photons at the output of the lens is

$$\delta t_{\text{out}} = \delta t_{\text{in}} + \frac{\pi V_m}{V_\pi}\omega_m^2\phi_o''\delta t_{\text{in}}. \tag{2}$$

When the three dispersive elements satisfy the lens equation [28]

$$-\frac{1}{\phi_l''} = \frac{1}{\phi_i''} + \frac{1}{\phi_o''}, \tag{3}$$

the output is a temporally magnified image of the input with magnification $M = \frac{\delta t_{\text{out}}}{\delta t_{\text{in}}} = -\frac{\phi_o''}{\phi_i''}$. The negative magnification implies that the time lens creates a temporally inverted image of the input photons. Note that similar to a spatial lens, a time lens has a finite aperture $\tau_a \approx \frac{1}{\omega_m}$ and therefore can be used only with pulsed light sources [28].

Our experiment was designed to achieve a magnification of ≈9.8×. The initial GDD was introduced by a 15-km spool of SMF-28 fiber with $\phi_i'' = -326$ ps^2. A large output GDD $\phi_o'' = -3190$ ps^2 corresponding to 150 km of SMF-28 was achieved by using a chirped Bragg grating (CBG). The EOM was driven by a rf signal with frequency $\nu_m = \frac{\omega_m}{2\pi} = 2.786$ GHz and was locked to the Ti:sapphire laser using a phase-locked loop (PLL). The π-phase-shift voltage V_π of the modulator was measured to be 3.49(6) V at 2.786 GHz. The rf signal amplitude V_m was set to 12.3 V, so that the GDD introduced by the EOM $\phi_l'' \approx 296$ ps^2 and satisfies the time-lens equation. Note that the GDD introduced by the lens is normal (positive), whereas that of input and output fibers is anomalous (negative). With these conditions, the lens is a converging lens [28].

III. RESULTS

A. Temporal magnification

To demonstrate the working and resolving power of our time lens, we first injected two photons into the lens, one arriving in *early* time bin t_e and the other arriving in *late* time bin t_l. The delay between the two time bins, $\delta t_{\text{in}} = t_l - t_e$, was tunable and was chosen to be 20–60 ps, smaller than the timing jitter (106 ps) of the detector, so that the two photons cannot be directly resolved. The two photons were generated using a type-II, collinear spontaneous parametric down-conversion (SPDC) process in a 30-mm periodically poled KTP (potassium titanyl phosphate) crystal pumped by a pulsed Ti:sapphire laser emitting ≈10-ps pulses at ≈775.45-nm wavelength [see Fig. 1(a)]. The crystal was phase matched to produce nearly degenerate, orthogonally polarized (H and V) signal and idler photons near 1550.9 nm, at 30 °C. These orthogonally polarized photons were separated using a polarization beam splitter (PBS), and a relative delay was introduced between them. The V polarized photons were converted to H polarized photons using a half-wave plate (HWP), and then the photons were recombined into a single-mode fiber using a fused-fiber beam splitter. The photons were subsequently filtered using a bandpass filter with a FWHM of ≈75 GHz (0.6 nm) and sent to the time lens. The lower bound on the photon pulse width was estimated to be 16.7(7) ps using Hong-Ou-Mandel (HOM) interference. The photons at the output of the time lens were detected using a SNSPD, and their arrival time was recorded using a time-interval analyzer [TIA; see Fig. 1(c)].

Figure 2(a) shows the observed photon pulses at the output of the lens for different input delays δt_{in} between the two photons. We can clearly resolve the two photons with an input delay as short as 23 ps, consistent with the estimated temporal resolution, the ratio of the effective focal length to the aperture of the lens, $\delta t_0 = \frac{2V_\pi}{V_m\omega_m} \approx 30$ ps [28]. Figure 2(b) plots the measured delay between photons at the output of the lens as a function of delay at the input. The slope of this linear plot is the magnification factor M, measured to be 9.6(2), in very

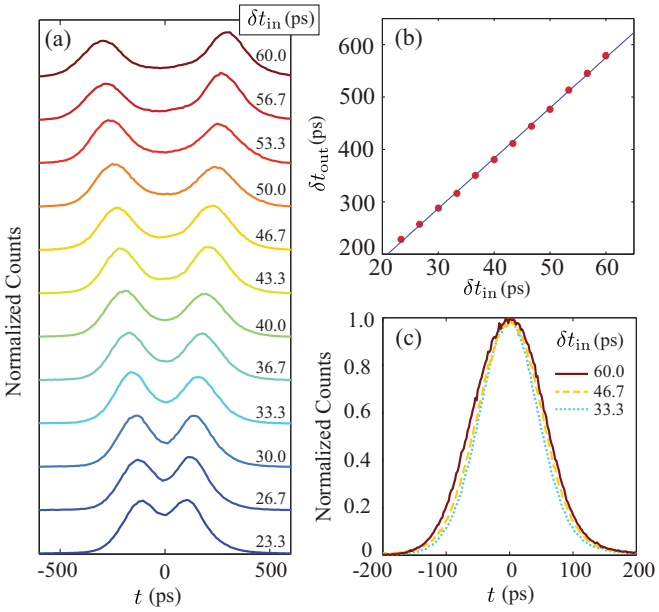

FIG. 2. (a) Observed photon pulses after the time lens for different input time delays δt_{in}. The two photons are very well resolved after the time lens for delay as small as ≈23 ps. (b) Measured delay (red circles) between photons at the output of the lens as a function of delay at the input. The delay increases linearly, with a slope $M = 9.6(2)$, where the uncertainty is from the linear fit (blue solid line). The size of the error bars, representing statistical error in finding peaks of photon pulses, is less than the size of the circles. (c) Because of the detector jitter (≈100 ps) of SNSPD, without the time lens, the two photons cannot be resolved even for delay δt_{in} as large as 60 ps.

good agreement with the design value of $M = 9.8$. The high fidelity of the time lens is evident from the linearity of the plot, which shows that the magnification is the same throughout the lens aperture. The small discrepancy between the observed and designed magnification factors is due to marginal overfilling of the time-lens aperture for higher δt_{in}. Furthermore, the measured individual photon pulse width (FWHM) at the lens output is 186(1) ps (after correcting for detector jitter), in good agreement with the observed magnification factor, given the input pulse width was estimated to be 16.7(7) ps. For comparison, Fig. 2(c) shows the observed TIA response when the photons are incident on the detector without a time lens, and the two photons are completely unresolved by the detector.

B. Measurement of temporal correlations

Simple measurements of the time delay between two photons, which are essentially projective measurements of the two-photon temporal wave function, do not provide any insight into quantum correlations. For example, single-channel delay measurements cannot distinguish between two-photon states corresponding to temporally bunched and antibunched photons [35]. In the bunched state $(|2_e,0_l\rangle - |0_e,2_l\rangle)$, both the photons arrive in the early time bin, or both arrive in the late time bin. In the antibunched state $(|1_e,1_l\rangle)$, one photon arrives early, and the other arrives late. An alternative is to measure the JTI, which can characterize temporal correlations of a two-photon state, analogous to the joint-spectral intensity (JSI), which is used to characterize spectral correlations between photon pairs [36]. JTI is the probability of finding two photons, one at time t_1 and the other at t_2, and is defined as $|\psi(t_1,t_2)|^2$, where $\psi(t_1,t_2)$ is the two-photon temporal wave function. Even though a JTI measurement does not measure the phase associated with the two-photon wave function, it is well suited for many quantum simulation techniques, for example, quantum walks and boson sampling, which require a measurement only of intensity correlations. JTI of a two-photon state can be easily measured using a beam splitter and time-resolved coincident detection events at two detectors [see Fig. 1(d)]. However, direct JTI measurements are limited in time resolution because of the detector jitter. While time-resolved frequency up-conversion [37] and intensity modulation [8] schemes allow JTI measurements with picosecond resolution by effectively introducing narrow filters in time or frequency, they require a two-dimensional scan of the filter position(s) for a two-photon state and therefore can be extremely slow. In the following, we demonstrate that a time lens expands the two-photon temporal wave function while preserving the quantum correlations of the wave function. This magnification allows us to directly measure the JTI, without any filtering, and hence reveal correlations of two-photon states with a resolution beyond the limitations imposed by detector jitter.

To generate two-photon states with bunched and antibunched temporal correlations, we use another HWP after the SPDC. When the HWP is set at an angle of 22.5° with respect to the horizontal, it acts as a 50:50 beam splitter for the H and V polarized photons. Furthermore, as shown in Refs. [38,39] and Appendix B, when the two-photon spectral wave function after the SPDC is symmetric with respect to the exchange of photons, the two-photon state after the HWP is polarization entangled, i.e., $|2_H,0_V\rangle - |0_H,2_V\rangle$. The PBS and the delay line following the HWP map this polarization-entangled state to the time-bin-entangled state

$$|\Psi_B\rangle = \iint dt_1 dt_2 \psi(t_1,t_2)[a^\dagger(t_1 - t_e)a^\dagger(t_2 - t_e) - e^{i\theta}a^\dagger(t_1 - t_l)a^\dagger(t_2 - t_l)]|0\rangle, \quad (4)$$

where $a^\dagger(t - t_{e(l)})$ is the photon creation operator corresponding to the early (late) time bin and θ is the phase resulting from delay δt_{in}. This is a time-bin-entangled two-photon state where the two photons are always bunched (B), appearing either in the early time bin t_e or in the late time bin t_l. Figure 3(a) shows the simulated JTI for this state, with the individual photon pulses assumed to be Gaussian. In our experiment, the exchange symmetry of the two-photon spectral wave function was confirmed using high-visibility (≈80%) HOM interference and a direct measurement of the JSI of the two photons using chirped Bragg grating as a frequency-to-time converter (Fig. 1) [36,39].

When the HWP angle is set to 0°, it does not mix the H and V polarized photons, and therefore, the two-photon state at the input of the lens is

$$|\Psi_{AB}\rangle = \iint dt_1 dt_2 \psi(t_1,t_2)a^\dagger(t_1 - t_e)a^\dagger(t_2 - t_l)|0\rangle. \quad (5)$$

Now, the two photons are antibunched (AB); that is, they always arrive in different time bins. Note that this state is

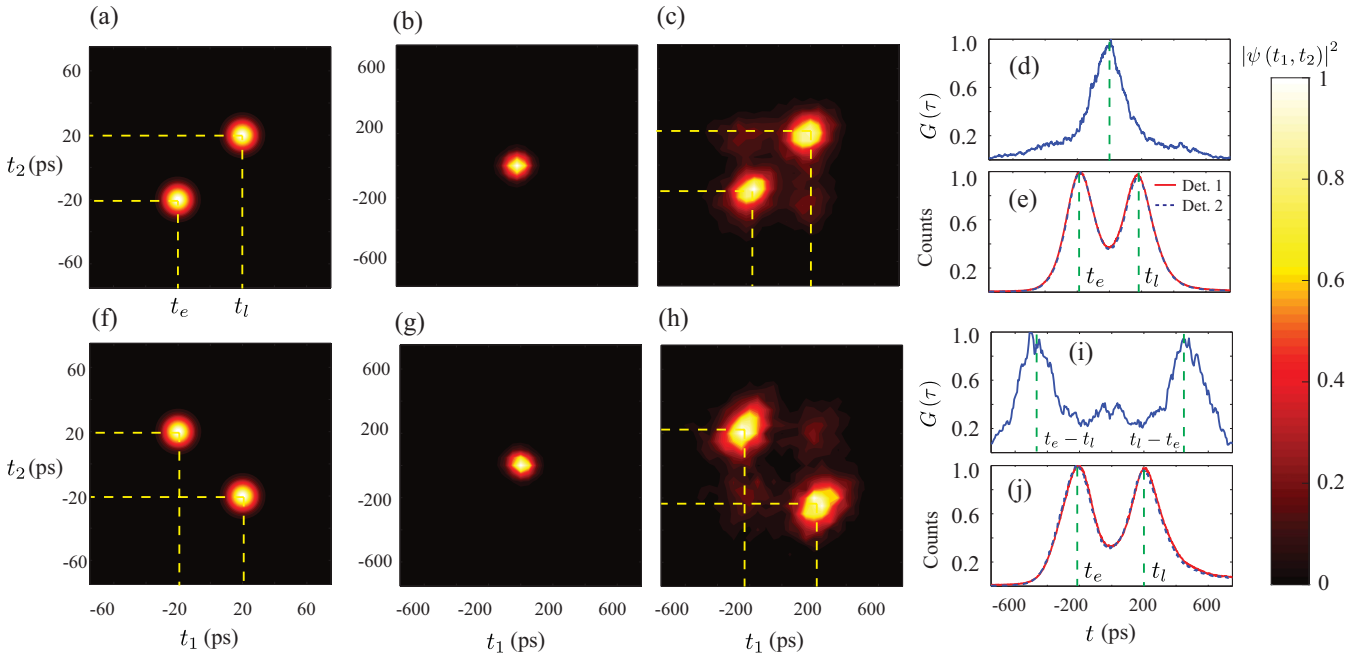

FIG. 3. (a) Simulated JTI of the bunched two-photon state before the time lens. (b) Measured JTI, without the time lens. The temporal correlations cannot be resolved at all. (c) Measured JTI with the time lens. The two photons can now be very clearly resolved, showing bunched behavior. (d) Measured $G(\tau)$ peaks at $\tau = 0$, consistent with bunched behavior. (e) Measured single-channel counts on two detectors. (f)–(j) Corresponding results for the antibunched state. $G(\tau)$ now peaks at $\tau = \pm(t_e - t_l) \approx 420$ ps, showing antibunched photons. Note that the single-channel measurements of photon pulses cannot distinguish between the two states.

not time bin entangled but the beam splitter used for JTI measurement after the lens cannot distinguish between the two photons and therefore induces entanglement (see Appendix B). The simulated JTI for this antibunched state is shown in Fig. 3(f).

Figures 3(b) and 3(c) show the measured JTI for the bunched state $|\Psi_B\rangle$, without and with a time lens, respectively. In the absence of a time lens, direct measurement of JTI [using the setup shown in Fig. 1(d)] cannot resolve any correlations in the two-photon state because the time bins are separated by a delay (40 ps) less than the timing jitter ($\approx$100 ps) of the two detectors. By using a time lens, we magnify the temporal correlations between the photons, which are now easily resolved by JTI measurements [Fig. 3(c)]. Good agreement of the measured JTI with the simulated JTI shows that the time lens faithfully magnifies the two-photon wave function while preserving its temporal correlations. A small probability of photons arriving in different time bins (antibunched, along the antidiagonal) is also observed in this plot. This is mainly because of multiphoton processes in the SPDC (see Appendix C). The measured delay between the time bins $\delta t \approx 360$ ps is consistent with the observed magnification.

To further quantify this behavior, in Fig. 3(d) we plot the probability $G(\tau)$ of photons arriving with a time difference τ, i.e.,

$$G(\tau) = \iint dt_1 dt_2 |\psi(t_1,t_2)|^2 \delta(\tau - t_1 + t_2). \qquad (6)$$

As can be seen, $G(\tau)$ peaks at $\tau = 0$ again verifying that the photons are bunched.

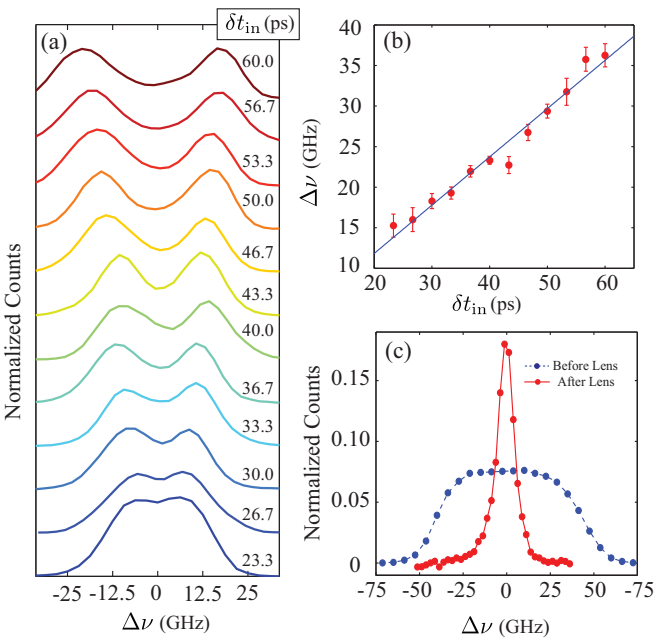

FIG. 4. (a) Measured spectrum of photon pulses for different input delay δt_{in}. (b) Relative frequency shift as a function of input delay δt_{in}. A linear fit (blue line) to the measured data (red circles) gives a slope of 0.60(8) and agrees well with the slope of 0.54 estimated using (1). (c) Measured spectral profile before the time lens (FWHM $\sim$ 75 GHz) and after the time lens (FWHM $\sim$ 9 GHz, corrected for a monochromator bandwidth of 8.2 GHz) gives a spectral compression factor of $\approx$8.3$\times$.

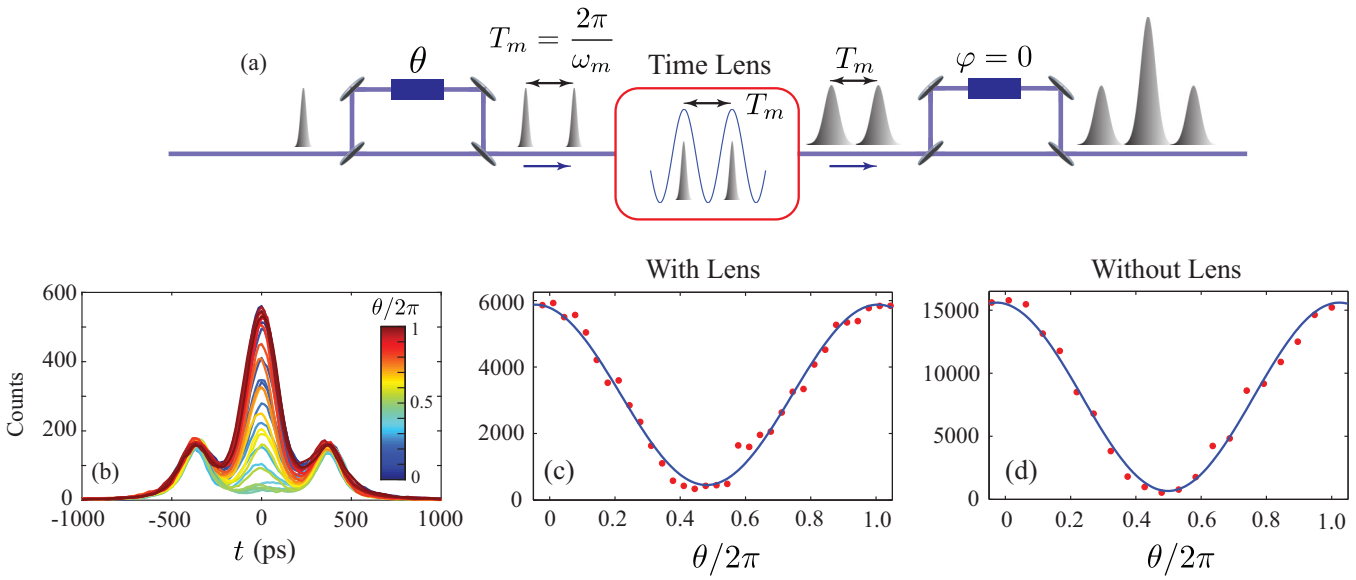

FIG. 5. (a) Setup used to test coherence of the time lens. A single photon is prepared in the superposition of *early* and *late* time bins, with a phase θ. The time difference between the early and late time bins is set to be equal to the time period of the rf drive (≈360 ps) for the EOM so that there is no relative frequency shift. At the output of the time lens, a Franson interferometer, with the same delay as the input interferometer, is used to measure the phase θ. (b) Observed signal at the output for different values of phase θ. (c) Intensity of the middle peak as a function of phase θ. The intensity varies as $\cos(\theta - \varphi)$, where φ is the phase associated with the output interferometer. (d) Intensity of the middle peak as a function of θ, without the time lens.

Figures 3(f)–3(i) show the corresponding results for the antibunched state $|\Psi_{AB}\rangle$. Again, without the time lens no correlations are observed in the JTI, whereas with the time lens we clearly see that the two photons always arrive in different time bins. The probability $G(\tau)$ now peaks at $\tau = \pm(t_l - t_e)$. Also, a finite probability of bunching (along the diagonal) is observed which is due to multiphoton processes in the SPDC. To further highlight the significance of JTI measurements, in Figs. 3(e) and 3(j), we plot the observed singles count on the two detectors for bunched and antibunched cases, respectively. The plots for the two states are exactly identical and have no information about their correlations. This confirms that single-channel delay measurements, in general, cannot be used to characterize two-photon states.

C. Measurement of spectral correlations

Now, we show that a time lens also maps temporal correlations of input photons to frequency correlations of outgoing photons. As shown in (1), the EOM introduces a frequency shift $\delta\nu$ between two photons separated by a temporal delay δt_{in} at its input. The CBG used after the EOM maps this frequency shift to time, which is then measured using the TIA. Because this frequency-to-time mapping is linear, the time axis in Figs. 3(c) and 3(h) could be easily rescaled to frequency using (2) and shows that the two-photon wave function at the lens output is also frequency bin entangled. To independently verify this frequency shift, we used a monochromator to measure the spectrum of photons at the lens output. Figure 4(a) shows the measured spectrum for different input delays δt, and Fig. 4(b) plots the frequency shift as a function of delay δt. As expected, frequency shift increases linearly with a slope of 0.60(8), which compares well with the slope of 0.54 estimated using (1). We also confirmed spectral compression of single photons, and Fig. 4(c) plots the measured single-photon spectrum before and after the time lens. The measured bandwidth is ≈75 GHz before the lens and 9(1) GHz after the lens, corresponding to a spectral compression of ≈8.3×.

D. Coherence of the time lens

As shown in Eq. (4), the early and late time bins are associated with a relative phase θ arising from the delay in the input interferometer. A high-fidelity time lens is expected to be coherent and preserve this relative phase. However, JTI measurements are insensitive to this relative phase and therefore do not show the coherence of the time lens. Furthermore, as shown in Fig. 4, photons in the early and late time bins acquire a relative frequency shift as they propagate through the time lens. Therefore, the standard state tomography procedure using Franson interferometers cannot measure this relative phase θ after the time lens. For the same reason, the fidelity of the two-photon state after the time lens cannot be accessed using HOM interference.

Nevertheless, to show the coherence of the time lens, we prepare a single photon in a superposition state of early and late time bins with relative phase θ, $|e\rangle + e^{i\theta}|l\rangle$, such that the delay between the two time bins is equal to the time period (≈360 ps) of the rf drive for the EOM [Fig. 5(a)]. With this arrangement, the two time bins get magnified using two separate time lenses, but there is no relative frequency shift between the time bins. Therefore, a Franson interferometer, with the same delay as the input, can be used to measure the relative phase θ after the time lens.

Figure 5(b) shows the measured temporal response at the output of the interferometer for different values of phase θ and fixed phase $\varphi = 0$ of the output interferometer. The middle

peak corresponds to interference of early photons taking a longer path and late photons taking a shorter path in the output interferometer. Figure 5(c) shows the intensity of this middle peak as a function of input phase θ. As expected, its intensity is proportional to $\cos(\theta - \varphi)$. The visibility of this interference fringe was measured to be ≈86%. Furthermore, using a large delay of 360 ps between the two time bins allows time-resolved detection of photons and therefore a measurement of phase θ without the time lens. Figure 5(d) shows the measured interference fringe without the time lens, with a visibility of ≈93%. The marginal reduction in interference visibility while using a time lens is mainly because of the temporal magnification of photons, which reduces the orthogonality between the two time bins. This observation of high-visibility single-photon interference at the output of the time lens clearly demonstrates that the temporal magnification is coherent and preserves the relative phase between early and late time bins.

IV. CONCLUSION

We have shown 9.6× temporal magnification of a two-photon temporal wave function using a deterministic, electro-optic-modulator-based time lens. In this demonstration, the time lens was driven at only 2.8 GHz, whereas commercially available EOMs can easily achieve 40-GHz operation. By using higher rf frequencies, this technique could easily be adapted to achieve much higher magnification and picosecond-scale temporal resolution, using existing single-photon detectors. Furthermore, we used a two-photon source entangled in two discrete time bins. However, our scheme is more general and can be used to measure arbitrary temporal correlations of multiphoton states, for example, those arising from temporal quantum walks.

ACKNOWLEDGMENTS

This research was supported by AFOSR MURI Grant No. FA95501610323, ONR, the Sloan Foundation, and the Physics Frontier Center at the Joint Quantum Institute. We thank T. Huber, J. Fan, and G. Solomon for fruitful discussions, Q. Quraishi for kindly providing the nanowire detectors, A. Migdall and S. Polyakov for the HydraHarp time-tagging module, and J. Bienfang for the high-power amplifier.

APPENDIX A: ACTION OF A TIME LENS ON A TWO-PHOTON WAVE FUNCTION

In this Appendix, we derive the relations governing the action of a time lens on a two-photon wave function. We start with a general two-photon state at the input of the lens

$$|\Psi\rangle = \iint dt_1 dt_2 \psi_{\text{in}}(t_1,t_2) a^\dagger(t_1) a^\dagger(t_2)|0\rangle, \tag{A1}$$

where $\psi_{\text{in}}(t_1,t_2)$ is the two-photon temporal wave function. Using two-dimensional (2D) Fourier transform, the temporal wave function can be written in the frequency domain as

$$\psi_{\text{in}}(t_1,t_2) = \frac{1}{2\pi} \iint d\omega_1 d\omega_2 e^{i\omega_1 t_1} e^{i\omega_2 t_2} \tilde{\psi}_{\text{in}}(\omega_1,\omega_2), \tag{A2}$$

where $\tilde{\psi}_{\text{in}}(\omega_1,\omega_2)$ is now the two-photon spectral wave function at the input.

Following Ref. [28], this two-photon wave function is first subject to an input group delay dispersion ϕ_i'' which results in a chirped temporal wave function $\psi_{\text{ch}}(t_1,t_2)$ given as

$$\psi_{\text{ch}}(t_1,t_2) = \frac{1}{2\pi} \iint d\omega_1 d\omega_2 e^{i\omega_1 t_1} e^{i\omega_2 t_2} \times e^{(-i\phi_i'' \frac{(\omega_1-\omega_0)^2}{2})} e^{(-i\phi_i'' \frac{(\omega_2-\omega_0)^2}{2})} \tilde{\psi}_{\text{in}}(\omega_1,\omega_2). \tag{A3}$$

Here, ω_0 is the central frequency of the spectral wave function.

After the input dispersion, the chirped two-photon wave function enters the EOM. The EOM adds a time-dependent phase $\phi_l(t) = -\frac{\pi V_m}{V_\pi} \cos(\omega_m t)$ to the wave function such that the two-photon wave function after the EOM is given as

$$\psi_{\text{EOM}}(t_1,t_2) = e^{(i\frac{\pi V_m}{2V_\pi}\omega_m^2 t_1^2)} e^{(i\frac{\pi V_m}{2V_\pi}\omega_m^2 t_2^2)} \psi_{\text{ch}}(t_1,t_2). \tag{A4}$$

Finally, photons are subject to a large GDD at the output (ϕ_o'') which acts as a frequency-to-time converter, and the temporal wave function at the output of the time lens is

$$\psi_{\text{out}}(t_1,t_2) = \frac{1}{2\pi} \iint d\omega_1 d\omega_2 \exp(i\omega_1 t_1) \exp(i\omega_2 t_2) \times e^{(-i\phi_o'' \frac{(\omega_1-\omega_0)^2}{2})} e^{(-i\phi_o'' \frac{(\omega_2-\omega_0)^2}{2})} \tilde{\psi}_{\text{EOM}}(\omega_1,\omega_2), \tag{A5}$$

where $\tilde{\psi}_{\text{EOM}}(\omega_1,\omega_2)$ is the Fourier transform of $\psi_{\text{EOM}}(t_1,t_2)$. Using the above equations, the temporal wave function at the output of the lens can easily be calculated for any general two-photon wave function at its input.

APPENDIX B: GENERATION OF TIME-BIN-ENTANGLED TWO-PHOTON STATES

In this Appendix we discuss the formalism to generate time-bin-entangled photons using a combination of a HWP, a PBS, and a delay line. We start with writing the two-photon state just after the SPDC as

$$\begin{aligned} |\Psi\rangle &= \iint d\omega_1 d\omega_2 \tilde{\psi}(\omega_1,\omega_2) a_H^\dagger(\omega_1) a_V^\dagger(\omega_2)|0\rangle \\ &= \iint dt_1 dt_2 \psi(t_1,t_2) a_H^\dagger(t_1) a_V^\dagger(t_2)|0\rangle, \end{aligned} \tag{B1}$$

where the temporal, $\psi(t_1,t_2)$, and spectral, $\tilde{\psi}(\omega_1,\omega_2)$, two-photon wave functions are related by the 2D Fourier transform.

Following SPDC, the two photons are subjected to a HWP. We first analyze the case when the HWP is oriented at an angle of 22.5° with respect to the horizontal axis and results in a time-bin-entangled state where the photons are always bunched [Eq. (4)]. The HWP acts as a 50:50 beam splitter for the H and V polarized photons and leads to the two-photon state

$$\begin{aligned} |\Psi\rangle = \iint d\omega_1 d\omega_2 \tilde{\psi}(\omega_1,\omega_2) [&a_H^\dagger(\omega_1) a_H^\dagger(\omega_2) \\ &- a_V^\dagger(\omega_1) a_V^\dagger(\omega_2) + a_V^\dagger(\omega_1) a_H^\dagger(\omega_2) - a_H^\dagger(\omega_1) a_V^\dagger(\omega_2)]|0\rangle. \end{aligned} \tag{B2}$$

When the two-photon spectral wave function associated with the SPDC process is symmetric, i.e., $\tilde{\psi}(\omega_1,\omega_2) = \tilde{\psi}(\omega_2,\omega_1)$,

the last two terms in the above expression cancel each other, and the two-photon state is simply [38,39]

$$|\Psi\rangle = \iint d\omega_1 d\omega_2 \tilde{\psi}(\omega_1,\omega_2)[a_H^\dagger(\omega_1)a_H^\dagger(\omega_2) - a_V^\dagger(\omega_1)a_V^\dagger(\omega_2)]|0\rangle. \quad \text{(B3)}$$

This is a polarization-entangled state of two photons where both the photons are either H polarized or V polarized. This phenomenon is similar to the usual HOM interference with a beam splitter where both the photons at the output of the beam splitter go into the same port [38,39]. Here, the two polarization modes H and V are analogous to the two spatial modes, and the HWP works as the beam splitter.

To map this polarization entanglement to time-bin entanglement, we use a polarization beam splitter (PBS) to separate the H and V polarized photons. We then introduce a relative delay, $\delta t_{\text{in}} = t_l - t_e$, between the two paths such that H polarization corresponds to the early time bin t_e and V corresponds to the late time bin t_l. Another HWP is then used to convert the V polarized photons to H. Subsequently, photons from both the arms are collected in two polarization-maintaining fibers (PMFs) and combined using a fused-fiber beam splitter. The two-photon state after the fiber beam splitter is

$$\begin{aligned}|\Psi\rangle &= \iint d\omega_1 d\omega_2 \tilde{\psi}(\omega_1,\omega_2)[e^{-i\omega_1 t_e}e^{-i\omega_2 t_e}a^\dagger(\omega_1)a^\dagger(\omega_2) \\ &\quad - e^{-i\omega_1 t_l}e^{-i\omega_2 t_l}a^\dagger(\omega_1)a^\dagger(\omega_2)]|0\rangle \\ &= \iint dt_1 dt_2 \psi(t_1,t_2)[a^\dagger(t_1-t_e)a^\dagger(t_2-t_e) \\ &\quad - a^\dagger(t_1-t_l)a^\dagger(t_2-t_l)]|0\rangle. \end{aligned} \quad \text{(B4)}$$

This is a time-bin-entangled two-photon state where the photons always arrive bunched, either at time t_e or at time t_l. We have dropped polarization indices in this state because now both the photons are always H polarized. The JTI for this state is shown in Fig. 3(a).

Next, we analyze the case when the HWP is set at an angle of 0°; that is, its axis is aligned with the horizontal and leads to the generation of an antibunched two-photon state [Eq. (5)]. With this setting, the HWP does not rotate the polarizations of the two photons, and therefore, the two-photon state after the HWP is the same as that generated by the SPDC. It imprints an overall π phase on the two-photon wave function which is inconsequential. As before, we associate H and V polarized photons with early and late time bins, and the two-photon state at the output of the beam splitter is

$$|\Psi\rangle = \iint dt_1 dt_2 \psi(t_1,t_2)a^\dagger(t_1-t_e)a^\dagger(t_2-t_l)|0\rangle.$$

Note that this state is not a time-bin-entangled state. It is simply a correlated, separable state of two photons where one comes early and the other comes late. However, for JTI measurements, we use another fiber beam splitter after the time lens. The two output ports of the beam splitter are each connected to single-photon detectors. The two-photon state after the beam splitters is given as

$$\begin{aligned}|\Psi\rangle &= \iint dt_1 dt_2 \psi(t_1,t_2) \\ &\quad \times [d_1^\dagger(t_1-t_e) - i d_2^\dagger(t_1-t_e)] \\ &\quad \times [d_1^\dagger(t_2-t_l) - i d_2^\dagger(t_2-t_l)]|0\rangle, \end{aligned} \quad \text{(B5)}$$

where $d_{1,2}^\dagger$ are the photon creation operators on detectors 1 and 2. A measurement of the coincident events on two detectors then projects this state to

$$\begin{aligned}|\Psi\rangle &= \iint dt_1 dt_2 \psi(t_1,t_2) \\ &\quad \times [d_1^\dagger(t_1-t_e)d_2^\dagger(t_2-t_l) + d_2^\dagger(t_1-t_e)d_1^\dagger(t_2-t_l)]|0\rangle. \end{aligned} \quad \text{(B6)}$$

This is a measurement-induced entangled state where the two photons are always antibunched. When detector 1 records an early event at time t_e, detector 2 records a late event at time t_l and vice versa. The simulated JTI for this state is shown in Fig. 3(f).

APPENDIX C: CONTRIBUTION OF MULTIPHOTON PROCESSES TO MEASURED JTI

In the experimentally measured JTI [Fig. 3(c)] we observe some antibunched photons at the lens output for ideally bunched photons at the input and vice versa. These photon pairs with correlations opposite to what was expected are because of multiphoton processes in the SPDC. To estimate this contribution, we begin with approximating the multiphoton state after the SPDC as [40]

$$\begin{aligned}|\Psi\rangle &= \sqrt{(1-p_1-p_2)}|0_H,0_V\rangle + \sqrt{p_1}|1_H,1_V\rangle \\ &\quad + \sqrt{p_2}|2_H,2_V\rangle, \end{aligned} \quad \text{(C1)}$$

where p_1, p_2 are the probabilities per pump pulse to generate one and two photon pairs, respectively. We assume that the probability for generation of more than two photon pairs is negligible. As detailed in the previous Appendixes, these photons are passed through a HWP and a PBS, assigned time bins t_e and t_l corresponding to H and V polarizations, respectively, by the delay line, and finally recombined using a fiber beam splitter. For simplicity, we consider the HWP angle to be 0° so that the ideal state will be an antibunched state. If the fiber coupling efficiency is η, the multiphoton state in the fiber is

$$\begin{aligned}|\Psi\rangle &\simeq \sqrt{\eta^2 p_1}|1_e,1_l\rangle + \sqrt{\eta^2(1-\eta)^2 p_2}(|2_e,0_l\rangle + |0_e,2_l\rangle) \\ &\quad + \sqrt{2\eta^3(1-\eta)p_2}(|2_e,1_l\rangle + |1_e,2_l\rangle) + \sqrt{\eta^4 p_2}|2_e,2_l\rangle. \end{aligned} \quad \text{(C2)}$$

Here, the state $|2_e,1_l\rangle$ represents the case when there are two photons in the early time bin and one photon in the late time bin and so on. Also, we have retained only those terms which have at least two photons and therefore can lead to coincidence counts at the two detectors. Using this relation, we see that the probability of detecting two photons in the early or late time

bin is

$$p(e,e) = p(l,l) = 2[\eta^2(1-\eta)^2 p_2 + 2\eta^3(1-\eta)p_2 + \eta^4 p_2] = 2\eta^2 p_2, \tag{C3}$$

and that for detecting one photon each in the early and late time bins is

$$p(e,l) \simeq \eta^2 p_1. \tag{C4}$$

The extra factor of 2 in Eq. (C3) is because of the beam splitter used for JTI measurements. Therefore, the relative probability of bunched to antibunched photons is

$$\frac{p(e,e)}{p(e,l)} = \frac{2p_2}{p_1}. \tag{C5}$$

In our experiment, the SPDC was pumped with 300 mW of power with $p_1 \approx 0.1$ and $p_2 = \frac{g_2(0)}{2} p_1^2 \approx 0.009$, where $g_2(0) \approx 1.8$ is the second-order intensity correlation function at zero delay. Therefore, the probability of detecting bunched events to antibunched events, for an ideally antibunched two-photon state, is ≈0.2. This agrees well with the experimental observation in Figs. 3(c) and 3(h).

[1] N. Gisin and R. Thew, Nat. Photonics **1**, 165 (2007).
[2] J.-W. Pan, Z.-B. Chen, C.-Y. Lu, H. Weinfurter, A. Zeilinger, and M. Żukowski, Rev. Mod. Phys. **84**, 777 (2012).
[3] J. Brendel, N. Gisin, W. Tittel, and H. Zbinden, Phys. Rev. Lett. **82**, 2594 (1999).
[4] M. Sasaki *et al.*, Opt. Express **19**, 10387 (2011).
[5] A. P. Vandevender and P. G. Kwiat, J. Mod. Opt. **51**, 1433 (2004).
[6] S. Tanzilli, W. Tittel, M. Halder, O. Alibart, P. Baldi, N. Gisin, and H. Zbinden, Nature (London) **437**, 116 (2005).
[7] P. Kolchin, C. Belthangady, S. Du, G. Y. Yin, and S. E. Harris, Phys. Rev. Lett. **101**, 103601 (2008).
[8] C. Belthangady, S. Du, C.-S. Chuu, G. Y. Yin, and S. E. Harris, Phys. Rev. A **80**, 031803 (2009).
[9] O. D. Odele, J. M. Lukens, J. A. Jaramillo-Villegas, C. Langrock, M. M. Fejer, D. E. Leaird, and A. M. Weiner, Opt. Express **23**, 21857 (2015).
[10] N. Matsuda, Sci. Adv. **2**, e1501223 (2016).
[11] M. Allgaier, V. Ansari, L. Sansoni, C. Eigner, V. Quiring, R. Ricken, G. Harder, B. Brecht, and C. Silberhorn, Nat. Commun. **8**, 14288 (2017).
[12] L. J. Wright, M. Karpiński, C. Söller, and B. J. Smith, Phys. Rev. Lett. **118**, 023601 (2017).
[13] H. J. Kimble, Nature (London) **453**, 1023 (2008).
[14] J. Lavoie, J. M. Donohue, L. G. Wright, A. Fedrizzi, and K. J. Resch, Nat. Photonics **7**, 363 (2013).
[15] M. Karpiński, M. Jachura, L. J. Wright, and B. J. Smith, Nat. Photonics **11**, 53 (2016).
[16] A. Aspuru-Guzik and P. Walther, Nat. Phys. **8**, 285 (2012).
[17] I. Carusotto and C. Ciuti, Rev. Mod. Phys. **85**, 299 (2013).
[18] M. J. Hartmann, J. Opt. **18**, 104005 (2016).
[19] C. Noh and D. G. Angelakis, Rep. Prog. Phys. **80**, 016401 (2017).
[20] K. R. Motes, A. Gilchrist, J. P. Dowling, and P. P. Rohde, Phys. Rev. Lett. **113**, 120501 (2014).
[21] Y. He, X. Ding, Z.-E. Su, H.-L. Huang, J. Qin, C. Wang, S. Unsleber, C. Chen, H. Wang, Y.-M. He, X.-L. Wang, W.-J. Zhang, S.-J. Chen, C. Schneider, M. Kamp, L.-X. You, Z. Wang, S. Höfling, C.-Y. Lu, and J.-W. Pan, Phys. Rev. Lett. **118**, 190501 (2017).
[22] M. Pant and D. Englund, Phys. Rev. A **93**, 043803 (2016).
[23] A. Schreiber, A. Gábris, P. P. Rohde, K. Laiho, M. Štefaňák, V. Potoček, C. Hamilton, I. Jex, and C. Silberhorn, Science **336**, 55 (2012).
[24] S. Mittal, V. V. Orre, and M. Hafezi, Opt. Express **24**, 15631 (2016).
[25] F. Marsili *et al.*, Nat. Photonics **7**, 210 (2013).
[26] C. M. Natarajan, M. G. Tanner, and R. H. Hadfield, Supercond. Sci. Technol. **25**, 063001 (2012).
[27] N. Calandri, Q.-Y. Zhao, D. Zhu, A. Dane, and K. K. Berggren, Appl. Phys. Lett. **109**, 152601 (2016).
[28] B. H. Kolner, IEEE J. Quantum Electron. **30**, 1951 (1994).
[29] C. V. Bennett and B. H. Kolner, Opt. Lett. **24**, 783 (1999).
[30] M. A. Foster, R. Salem, D. F. Geraghty, A. C. Turner-Foster, M. Lipson, and A. L. Gaeta, Nature (London) **456**, 81 (2008).
[31] M. A. Foster, R. Salem, Y. Okawachi, A. C. Turner-Foster, M. Lipson, and A. L. Gaeta, Nat. Photonics **3**, 581 (2009).
[32] J. M. Donohue, M. Mastrovich, and K. J. Resch, Phys. Rev. Lett. **117**, 243602 (2016).
[33] J. M. Donohue, M. Agnew, J. Lavoie, and K. J. Resch, Phys. Rev. Lett. **111**, 153602 (2013).
[34] S. Ramelow, L. Ratschbacher, A. Fedrizzi, N. K. Langford, and A. Zeilinger, Phys. Rev. Lett. **103**, 253601 (2009).
[35] W. Tittel, J. Brendel, H. Zbinden, and N. Gisin, Phys. Rev. Lett. **81**, 3563 (1998).
[36] G. Harder, V. Ansari, B. Brecht, T. Dirmeier, C. Marquardt, and C. Silberhorn, Opt. Express **21**, 13975 (2013).
[37] O. Kuzucu, F. N. C. Wong, S. Kurimura, and S. Tovstonog, Phys. Rev. Lett. **101**, 153602 (2008).
[38] P. S. Kuo, T. Gerrits, V. B. Verma, and S. W. Nam, Opt. Lett. **41**, 5074 (2016).
[39] T. Gerrits, F. Marsili, V. B. Verma, L. K. Shalm, M. Shaw, R. P. Mirin, and S. W. Nam, Phys. Rev. A **91**, 013830 (2015).
[40] D. F. Walls and G. J. Milburn, *Quantum Optics* (Springer, Berlin, 2008).